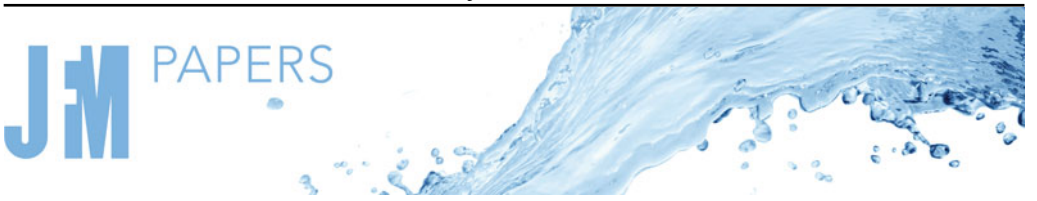
J. Fluid Mech. (2025), *vol.* 1008, A23, doi:10.1017/jfm.2025.115



Cascades transition in generalised two-dimensional turbulence

Vibhuti Bhushan Jha[1,2], **Kannabiran Seshasayanan**[2] and **Vassilios Dallas**[3,4]

[1]Space Applications Centre, Indian Space Research Organisation, Ahmedabad, Gujarat, India

[2]Department of Applied Mechanics, Indian Institute of Technology Madras, Chennai, India

[3]Mathematical Institute, University of Oxford, Oxford OX2 6GG, UK

[4]Environmental Research Laboratory, National Centre for Scientific Research "Demokritos", 15341 Athens, Greece

Corresponding authors: Vibhuti Bhushan Jha, vibhutibjha@gmail.com; Kannabiran Seshasayanan, kanna@iitm.ac.in; Vassilios Dallas, vassilios.dallas@gmail.com

(Received 22 December 2023; revised 23 November 2024; accepted 14 January 2025)

Generalised two-dimensional (2-D) fluid dynamics is characterised by a relationship between a scalar field q, called generalised vorticity, and the stream function ψ,namely $q = (-\nabla^2)^{\frac{\alpha}{2}}\psi$. We study the transition of cascades in generalised 2-D turbulence by systematically varying the parameter α and investigating its influential role in determining the directionality (inverse, forward or bidirectional) of these cascades. We derive upper bounds for the dimensionless dissipation rates of generalised energy E_G and enstrophy Ω_G as the Reynolds number tends to infinity. These findings corroborate numerical simulations, illustrating the inverse cascade of E_G and forward cascade of Ω_G for $\alpha > 0$, contrasting with the reverse behaviour for $\alpha < 0$. The dependence of dissipation rates on system parameters reinforces these observed transitions, substantiated by spectral fluxes and energy spectra, which hint at Kolmogorov-like scalings at large scales but discrepancies at smaller scales between numerical and theoretical estimates. These discrepancies are possibly due to non-local transfers, which dominate the dynamics as we go from positive to negative values of α. Intriguingly, the forward cascade of E_G for $\alpha < 0$ reveals similarities to three-dimensional turbulence, notably the emergence of vortex filaments within a 2-D framework, marking a unique feature of this generalised model.

Key words: quasi-geostrophic flows, nonlinear instability, Navier–Stokes equations

© The Author(s), 2025. Published by Cambridge University Press. This is an Open Access article, distributed under the terms of the Creative Commons Attribution licence (https://creativecommons.org/licenses/by/4.0/), which permits unrestricted re-use, distribution and reproduction, provided the original article is properly cited.

https://doi.org/10.1017/jfm.2025.115 Published online by Cambridge University Press

1. Introduction

The presence of nonlinear interactions allows energy to be transferred across different length scales in turbulent flows. While in three-dimensional (3-D) turbulence, energy is transferred to small scales (forward cascade), energy is transferred to large scales in two-dimensional (2-D) turbulence (inverse cascade). This, along with the existence of a second quadratic invariant, makes 2-D turbulence an exciting system. Not limited to theoretical or numerical studies, such behaviour has been observed in atmospheric (Lilly 1969; Rhines 1979; Nastrom *et al.* 1984; Read 2001) and planetary flows (Siegelman *et al.* 2022). The presence of external mechanisms like rotation, stratification, magnetic field or compactification of one dimension can make the prediction of the cascade direction challenging (Celani *et al.* 2010; Alexakis 2011; Sen *et al.* 2012; Marino *et al.* 2013; Deusebio *et al.* 2014). This is due to the competing behaviour between the forward and inverse cascades of the quadratic invariants, often dependent on some control parameter like anisotropy, rotation rate, etc. This results in bidirectional cascades of the quadratic invariants. Such bidirectional cascades have been observed in numerical (Smith *et al.* 1996; Alexakis 2011; Seshasayanan *et al.* 2014*a*; Sozza *et al.* 2015) and experimental settings (Shats *et al.* 2010; Xia *et al.* 2011; Campagne *et al.* 2014). Furthermore, there is evidence for bidirectional cascades in atmospheric (Byrne & Zhang 2013; King *et al.* 2015; Shao *et al.* 2023), oceanic (Scott & Wang 2005; Arbic *et al.* 2013; Balwada *et al.* 2016; Khatri *et al.* 2018; Balwada *et al.* 2022) and planetary flows (Lesur & Longaretti 2011; Young & Read 2017).

The transition from one type of cascade to another can be either smooth or occur at a critical point (Alexakis & Biferale 2022; Alexakis 2023; van Kan 2024). The presence of a critical dimension at which the cascade direction changes has been demonstrated by Frisch *et al.* (1976) and recently examined further by Verma (2024). Benavides & Alexakis (2017) found the transition from a forward to a bidirectional cascade of energy in thin layers of fluid turbulence to be critical (Ecke 2017). In 2-D magnetohydrodynamic (MHD) turbulence, the variation in magnetic field strength above a critical value leads to cascades transition of the quadratic invariants (Seshasayanan *et al.* 2014*a*), and the inverse energy flux scales as a power law. Similarly under certain regimes, MHD flows can behave like a 2-D flow at large scales and 3-D flow at smaller scales (Alexakis 2011). In this case, the inverse cascade of energy is highly sensitive to the strength of the magnetic field.

Pierrehumbert *et al.* (1994*a*) considered a generalised model of 2-D turbulence characterised by a parameter α which links the streamfunction to a scalar field called generalised vorticity. Certain values of α lead to equations relevant in the context of geophysical flows. For $\alpha = 2$, the generalised model gives the familiar barotropic vorticity equation from 2-D Navier–Stokes (Tabeling 2002; Boffetta & Ecke 2012). For $\alpha = 1$, it gives the surface quasi-geostrophic (SQG) equation, which describes the motion of a rotating stratified fluid (Held *et al.* 1995*a*; Lapeyre 2017). For $\alpha = -2$, it gives a rescaled shallow-water quasi-geostrophic equation in the asymptotic limit of length scales large compared with the deformation scale (Larichev & McWilliams 1991; Smith *et al.* 2002). In generalised 2-D turbulence, changing the value of α leads to varying degrees of forward and inverse cascades of the quadratic invariants. There are various studies using different values of α and analysing the associated energy spectra (Tran 2004; Watanabe & Iwayama 2004; Iwayama *et al.* 2015).

Two-dimensional instabilities can couple the forced modes to large-scale 2-D modes, transferring energy to larger scales, which indicate the possibility of an inverse cascade (Alexakis 2018). This non-local interaction of scales can be quantified with the notion of negative eddy viscosity (Kraichnan 1976). The cascades of 2-D Navier–Stokes turbulence

https://doi.org/10.1017/jfm.2025.115 Published online by Cambridge University Press

($\alpha = 2$) have been predicted to be less local than for 3-D turbulence (Kraichnan 1971; Boffetta & Ecke 2012). Pierrehumbert *et al.* (1994*a*) focus on positive values of α only and argue that $\alpha = 2$ is at the transition between local to non-local transfers of generalised enstrophy, in the sense that dominant straining of small scales comes from the largest scales when $\alpha > 2$. However, Watanabe & Iwayama (2007), Foussard *et al.* (2017) found non-local interactions in the generalised enstrophy transfer for $1 \leqslant \alpha \leqslant 2$. For the energy transfers, Pierrehumbert *et al.* (1994*a*) argued that they become non-local when $\alpha > 4$.

The value of α decides the nature of the cascades. For positive α, energy (enstrophy) cascades to large (small) scales, whereas energy (enstrophy) cascades to small (large) scales for negative α. Thus, depending on the sign and value of α, the cascade would either be inverse, forward or bidirectional. This suggests that there is a transition in the direction of the cascades as one changes the value of α. It is also to be noted that the aforementioned studies have not analysed systematically the $\alpha < 0$ regime.

In this work, we focus on the numerical study of the cascades in generalised 2-D turbulence by systematically varying α in the range $-1 \leqslant \alpha \leqslant 2$. While it may be possible to extend the runs to values of $\alpha < -1$, it is computationally challenging to achieve a statistically stationary regime in the range of parameters we have considered in this study. We perform direct numerical simulation (DNS) to determine the transition of the cascades and we use exact mathematical inequalities to derive bounds on generalised energy and enstrophy dissipation rates. Finally, our study deals with the degree of non-locality of triadic interactions by analysing shell-to-shell transfers in the range $-1 \leqslant \alpha \leqslant 2$.

The paper is organised as follows. In § 2, we discuss the problem formulation. We present the numerical results in §§ 3 and 4, we discuss the theoretical bounds on the generalised energy and enstrophy dissipation rates that we derive in Appendix C. Finally, we summarise our concluding remarks in § 5.

2. Problem formulation

Consider the 2-D evolution equation of the generalised vorticity $q(x, y, t)$ in a periodic domain of size $[0, 2\pi] \times [0, 2\pi]$,

$$\partial_t q + J(q, \psi) = -\nu_+ \left(-\nabla^2\right)^n q - \nu_- \left(-\nabla^2\right)^{-m} q + f_q, \tag{2.1}$$

where $\psi(x, y, t)$ is the streamfunction, the nonlinear term is given by the Jacobian $J(q, \psi) = \partial_x q \partial_y \psi - \partial_x \psi \partial_y q$, ν_+ is the hyper-viscous coefficient, ν_- is the hypo-viscous coefficient and f_q is the external forcing. The fluid velocity is given by $\mathbf{u} = \nabla \times (\psi \hat{z})$. The generalised relationship between q and ψ in 2-D fluid dynamics is

$$q = \left(-\nabla^2\right)^{\frac{\alpha}{2}} \psi, \tag{2.2}$$

as discussed by Pierrehumbert *et al.* (1994*b*), Smith *et al.* (2002), Tran (2004) and Teitelbaum & Mininni (2012).

In the presence of an inverse cascade, the energy of the large-scale modes grow to extreme values forming a condensate, the growth saturates when the viscous dissipation at the largest scale balances the energy injection (Tabeling 2002; Chan *et al.* 2012). To prevent the formation of a very large condensate and to reach a turbulent stationary regime, we supplement our system with a large-scale dissipative term $-\nu_-(-\nabla^2)^{-m} q$ that is responsible for saturating the inverse cascade. To model very-high-Reynolds-number flows, we consider a hyper-viscous term $-\nu_+(-\nabla^2)^n q$ by raising the Laplacian to an integer power $n > 1$. This term provides a wider inertial range, as it sets in at much smaller scales compared with the normal viscous term (with $n = 1$). The hypo-viscous term similarly extends the inertial range for scales larger than the forcing scale.

https://doi.org/10.1017/jfm.2025.115 Published online by Cambridge University Press

We denote the dimensions of a quantity by using the square bracket $[\cdot]$. Considering the fact that the variables x, y have units of length $[L]$, and t has units of time $[T]$, then $[\psi] = [L]^2[T]^{-1}$ and $[q] = [L]^{2-\alpha}[T]^{-1}$. Using (2.2), we define f_ψ, the forcing acting on the streamfunction equation with f_q as $f_q = (-\nabla^2)^{\frac{\alpha}{2}} f_\psi$. Taking f_0 to be the amplitude of f_ψ, the two dimensionless control parameters are the small-scale Reynolds number

$$Re_+ = \sqrt{f_0 k_f}/\left(\nu_+ k_f^{2n-1/2}\right), \tag{2.3}$$

and the large-scale Reynolds number

$$Re_- = \sqrt{f_0 k_f}/\left(\nu_- k_f^{-2m-1/2}\right), \tag{2.4}$$

with $[f_0] = [L]^2[T]^{-2}$, $[\nu_+] = [L]^{2n}[T]^{-1}$ and $[\nu_-] = [L]^{-2m}[T]^{-1}$.

In the limit of $\nu_+ \to 0$, $\nu_- \to 0$ and $f_q = 0$, the integral over a periodic domain of any function of the scalar field q is formally conserved. Therefore, there are infinite number of invariants (Smith *et al.* 2002). Following the Kolmogorov–Kraichnan phenomenology of 2-D Navier–Stokes turbulence, the two quadratic invariants that determine the cascade directions in generalised 2-D turbulence are

$$E_G = \frac{1}{2}\langle \psi q \rangle, \quad \Omega_G = \frac{1}{2}\langle q^2 \rangle, \tag{2.5}$$

where we refer to E_G as the generalised energy and Ω_G as the generalised enstrophy with units $[E_G] = [L]^{4-\alpha}[T]^{-2}$ and $[\Omega_G] = [L]^{4-2\alpha}[T]^{-2}$. The angular brackets $\langle\cdot\rangle$ denote spatiotemporal averaging. Multiplying (2.1) by ψ and integrating over space and time, we can derive the evolution equation of the generalised energy. Setting $dE_G/dt = 0$ due to statistical stationarity, we get

$$\epsilon = \epsilon_+ + \epsilon_-, \tag{2.6}$$

where $\epsilon_+ = \nu_+ \langle \psi (-\nabla^2)^n q \rangle$ is the small-scale dissipation rate, $\epsilon_- = \nu_- \langle \psi (-\nabla^2)^{-m} q \rangle$ is the large-scale dissipation rate and $\epsilon = \langle \psi f_q \rangle$ is the injection rate of the generalised energy. Similarly, if we multiply (2.1) with q and integrate over space and time, we obtain the evolution equation of the generalised enstrophy. Setting $\mathrm{d}\Omega_G/\mathrm{d}t = 0$ due to statistical stationarity, we get

$$\xi = \xi_+ + \xi_-, \tag{2.7}$$

where $\xi_+ = \nu_+ \langle q (-\nabla^2)^n q \rangle$ is the small-scale dissipation rate, $\xi_- = \nu_- \langle q (-\nabla^2)^{-m} q \rangle$ is the large-scale dissipation rate and $\xi = \langle q f_q \rangle$ is the injection rate of the generalised enstrophy.

The equivalent expression of (2.2) in Fourier space is

$$\widehat{q}(\mathbf{k}, t) = k^\alpha \widehat{\psi}(\mathbf{k}, t), \tag{2.8}$$

where $k = \sqrt{k_x^2 + k_y^2}$ is the isotropic two-dimensional wavenumber. The notation $\widehat{\cdot}$ denotes the Fourier transform coefficients. The spectra of the two quadratic invariants can be connected using the relationship (2.8) to get

$$\Omega_G(k) = k^\alpha E_G(k). \tag{2.9}$$

Now, the spectra of the two quadratic invariants in the inertial range can be derived following Kolmogorov (1941) scaling arguments, where the spectral flux is assumed to be constant in the inertial range, and the spectral densities $E_G(k)$ and $\Omega_G(k)$ are only

https://doi.org/10.1017/jfm.2025.115 Published online by Cambridge University Press

functions of the local scale and spectral flux. Hence, using dimensional arguments for the generalised energy and enstrophy, we get

$$\frac{kE_G(k)}{\tau_E(k)} = \epsilon = \text{const.}, \quad \tau_E(k) = \left[k^{5-\alpha} E_G(k)\right]^{-1/2}, \tag{2.10}$$

$$\frac{k\Omega_G(k)}{\tau_\Omega(k)} = \xi = \text{const.}, \quad \tau_\Omega(k) = \left[k^{5-2\alpha} \Omega_G(k)\right]^{-1/2}, \tag{2.11}$$

where $\tau_E(k)$ is the local turnover timescale that it takes to transfer $E_G(k)$ across the wavenumber shell k. Similarly, $\tau_\Omega(k)$ is the local turnover time scale to transfer $\Omega_G(k)$ across k. Then, by using (2.10), (2.11) and (2.9), we can obtain the following power laws for $\alpha > 0$:

$$E_G(k) \propto \epsilon^{2/3} k^{(\alpha-7)/3} \quad \text{for } k_{min} \ll k \ll k_f, \tag{2.12}$$

$$E_G(k) \propto \xi^{2/3} k^{(-\alpha-7)/3} \quad \text{for } k_f \ll k \ll k_{max}, \tag{2.13}$$

with the two wavenumber regimes denoting the inertial ranges above and below the intermediate forcing wavenumber k_f, respectively. Similarly, for $\alpha < 0$, the power laws remain unaltered, while their wavenumber range of validity is interchanged between (2.12) and (2.13). In a similar fashion, we can derive the power laws for the enstrophy spectra using (2.9).

The flux Π is a measure of the nonlinear cascade of a conserved quantity in turbulence (Alexakis & Biferale 2018). The energy flux across a circle of radius k in the 2-D wavenumber space is the total energy transferred from the modes within the circle to the modes outside the circle. Consequently, we define the flux of generalised energy $\Pi_E(k, t)$ and enstrophy $\Pi_\Omega(k, t)$ as

$$\Pi_E(k, t) = \sum_{k' \leqslant k} T_E(k', t), \tag{2.14a}$$

$$\Pi_\Omega(k, t) = \sum_{k' \leqslant k} T_\Omega(k', t), \tag{2.14b}$$

where $T_E(k, t)$ and $T_\Omega(k, t)$ are the nonlinear generalised energy and enstrophy transfers across k

$$T_E(k, t) = \sum_{k \leqslant |\mathbf{k}| < k+\Delta k} \widehat{\psi}^*(\mathbf{k}, t) \widehat{J(q, \psi)}(\mathbf{k}, t), \tag{2.15a}$$

$$T_\Omega(k, t) = \sum_{k \leqslant |\mathbf{k}| < k+\Delta k} \widehat{q}^*(\mathbf{k}, t) \widehat{J(q, \psi)}(\mathbf{k}, t), \tag{2.15b}$$

where the sum is performed over the Fourier modes with wavenumber amplitude k in a shell of width $\Delta k = 1$.

In general, we cannot determine the direction of cascade of two quadratic invariants unless there are special relations between the two like (2.9). A generalised Fjørtoft (1953) argument on the directions of the cascades of two quadratic invariants A and B, with energy spectra $E_A(k)$ and $E_B(k)$, has been formulated by Alexakis & Biferale (2022), which states that if there exists a constant $c > 0$ and an exponent $\beta > 0$, such that $E_A(k)$ and $E_B(k)$ satisfy

https://doi.org/10.1017/jfm.2025.115 Published online by Cambridge University Press

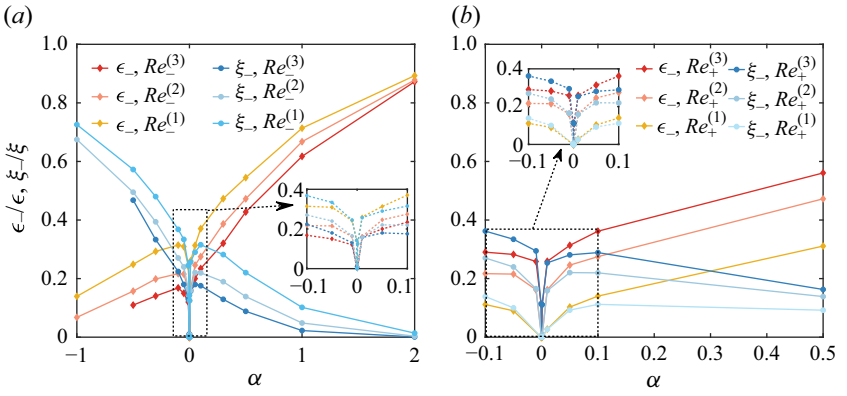


Figure 1. Normalised large-scale dissipation rate of generalised energy ϵ_-/ϵ and enstrophy ξ_-/ξ as a function of α. (*a*) Bifurcation diagram for fixed $Re_+ = 1381$ and increasing values of Re_-, where $Re_-^{(1)} = 10^6$, $Re_-^{(2)} = 4 \times 10^7$ and $Re_-^{(3)} = 2 \times 10^9$. (*b*) Bifurcation diagram for fixed $Re_- = 4 \times 10^7$ and increasing value of Re_+, where $Re_+^{(1)} = 345$, $Re_+^{(2)} = 1381$ and $Re_+^{(3)} = 3450$.

(i) $|E_A(k)| \leqslant ck^{-\beta} E_B(k)$, then A cannot cascade forward; or
(ii) $|E_B(k)| \leqslant ck^{\beta} E_A(k)$, then B cannot cascade inversely.

In other words, when $\alpha > 0$, then E_G is transferred towards large scales while Ω_G is transferred towards small scales. The opposite is true when $\alpha < 0$. In Appendix C, we demonstrate this rigorously using mathematical inequalities on the dissipation rates of the generalised energy and enstrophy for positive and negative values of α separately.

3. Numerical results

We numerically integrate (2.1) to investigate the transition of the cascades, for high Reynolds numbers, by varying α systematically in the range $-1 \leqslant \alpha \leqslant 2$. The domain is taken to be periodic in both directions with dimensions $[0, 2\pi] \times [0, 2\pi]$. The external forcing we use to drive the flows is time-independent, monochromatic and takes the form $f_q = (-\nabla^2)^{\frac{\alpha}{2}} f_\psi$ with $f_\psi = f_0 \sin(k_f x) \sin(k_f y)$, where f_0 denotes the amplitude of the forcing and k_f the forcing wavenumber. In our simulations, we choose $n = 2$ for the hyper-viscous term and $m = 2$ for the hypo-viscous term. The details of the numerical method and simulation parameters used are described in Appendix A.

3.1. *Transition of generalised energy and enstrophy cascades*

Using the large-scale dissipation rates $\epsilon_- = \nu_- \langle \psi \nabla^{-4} q \rangle$ and $\xi_- = \nu_- \langle q \nabla^{-4} q \rangle$, we quantify the variation in the generalised energy and enstrophy fluxes to large scales. For the parameters explored, ϵ_- and ξ_- are localised at large length scales giving an estimate of the flux to large scales occurring through an inverse cascade.

In figure 1, we show the large-scale dissipation rates normalised by their respective injection rates, ϵ_-/ϵ and ξ_-/ξ, as a function of α. The normalised large- and small-scale quantities are related by the expression $(\epsilon_-/\epsilon) = 1 - (\epsilon_+/\epsilon)$ from (2.6) and $(\xi_-/\xi) = 1 - (\xi_+/\xi)$ from (2.7). In figure 1(*a*), we consider different values of Re_- with fixed Re_+, while in figure 1(*b*), we consider different values of Re_+ with fixed Re_-. We find that for $\alpha = 2$, the energy dissipation is predominantly at large-length scales due to the inverse cascade of energy in 2-D Navier–Stokes turbulence. However, for $\alpha = -1$, we observe

https://doi.org/10.1017/jfm.2025.115 Published online by Cambridge University Press

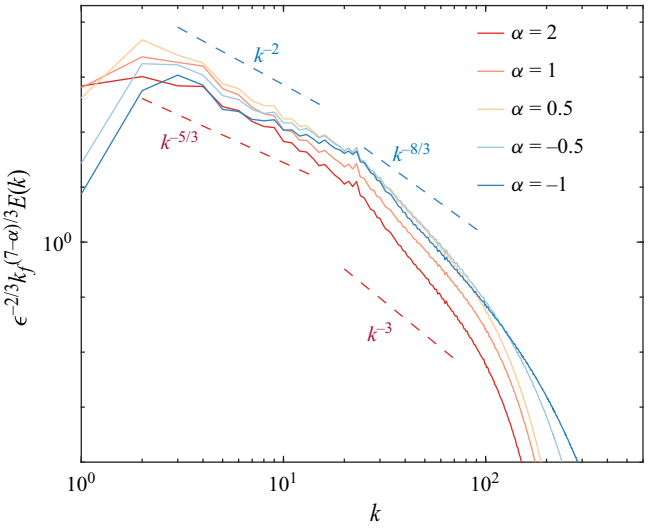


Figure 2. Compensated energy spectra for different α along with their theoretical exponents in red ($\alpha = 2$) and blue ($\alpha = -1$) are shown as dashed lines. The spectra are obtained from DNS with $Re_+ = 1381$, $Re_- = 4 \times 10^7$ and $k_f = 16\sqrt{2}$.

the transition of the cascades with the energy to be predominantly dissipated at small scales suggesting a forward cascade of energy. For intermediate values of α, we find that energy is dissipated at both large and small scales implying the presence of a bidirectional cascade.

As seen from figure 1(*a*), increasing Re_- for a given Re_+ leads to weaker inverse cascades of both the generalised energy and enstrophy. In figure 1(*b*), increasing Re_+ for a fixed Re_- leads to smaller forward cascade of both the generalised energy and enstrophy. So, the cascades of generalised energy and enstrophy depend on the values of Re_+ and Re_- we have considered. Further studies focusing on particular values of α and systematically increasing Re_+ and Re_- could shed light on whether the dissipation rates become finite or not in the limit of infinite Reynolds.

Close to $\alpha = 0$, we find that the behaviour depends strongly on the control parameters Re_+ and Re_- as the nonlinearity, which leads to the cascade, diminishes as $\alpha \to 0$. At $\alpha = 0$, there is no cascade as the nonlinearity vanishes, i.e. $J(\psi, \psi) = 0$ by definition. Hence, both the forcing and dissipation are localised at the wavenumber k_f. For low enough values of $|\alpha|$, temporal chaotic behaviour is observed. However, based on the energy spectrum, we find turbulent flows for $\alpha \gtrsim 0.001$ and $\alpha \lesssim -0.001$ in our numerical simulations. We refer to $\alpha = 0$ as the threshold where the cascades vanish for any value of Re_+ and Re_-. For the simulation parameters that are explored here, the small-scale dissipation dominates over the large-scale dissipation near $\alpha \approx 0$ implying that the dissipation due to large-scale friction is negligible, and thus $\epsilon_-/\epsilon \ll 1$. The exact behaviour close to $\alpha = 0$ will be discussed in § 3.2.

In figure 2, we show the generalised energy spectrum for different values of α. The dashed lines show the phenomenological predictions from (2.12) and (2.13). The red dashed lines show the predictions for $\alpha = 2$ and the blue dashed lines show the predictions for $\alpha = -1$. We see that the generalised energy spectra in the range $k_{min} < k < k_f$ have exponents close to the predictions (2.12), while in the range $k_f < k < k_{max}$, the exponents are far from the phenomenological predictions. This discrepancy might arise

https://doi.org/10.1017/jfm.2025.115 Published online by Cambridge University Press

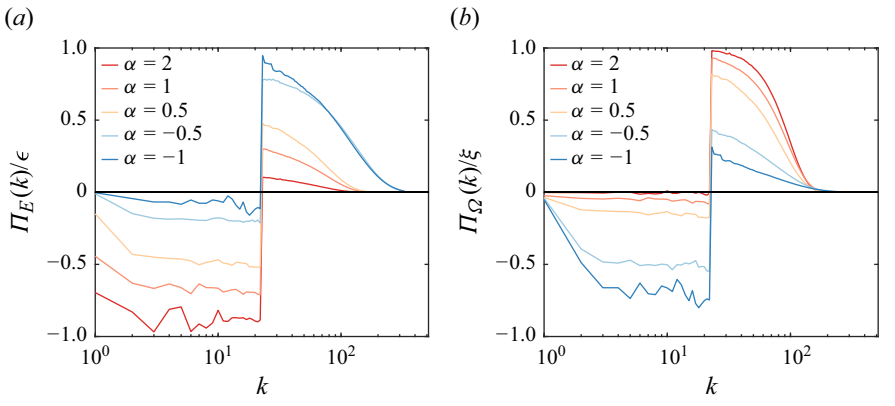


Figure 3. (*a*) Normalised energy flux and (*b*) normalised enstrophy flux for different α. The fluxes are obtained from DNS with $Re_+ = 1381$, $Re_- = 4 \times 10^7$ and $k_f = 16\sqrt{2}$.

out of intermittency effects (Ishihara *et al.* 2009). In particular, for the 2-D Navier–Stokes turbulence ($\alpha = 2$), Boffetta & Musacchio (2010) report that the exponent in the range $k_f < k < k_{max}$ depends on the small-scale Reynolds number. Simulations at higher resolutions are required to shed light on the differences between the spectral exponents from DNS for the different values of α and the Kolmogorov-like scalings from (2.12) and (2.13).

Figure 3 shows the fluxes of generalised energy and enstrophy, normalised with their respective injection rates, for different values of α. For the Navier–Stokes model ($\alpha = 2$), we see that E_G cascades mostly to large scales (or low k), while Ω_G cascades mostly to small scales (or high k). For $\alpha = -1$, we find the opposite scenario where E_G mostly cascades to small scales while Ω_G cascades to large scales. Intermediate values of α show bidirectional cascades, where E_G and Ω_G cascade to both large and small scales. This transition of cascades is similar to those observed in other turbulent systems (Celani *et al.* 2010; Seshasayanan *et al.* 2014*b*; Benavides & Alexakis 2017; van Kan & Alexakis 2020).

Generally, a bidirectional cascade can be observed if the dynamical properties of the flow at wavenumbers $k \ll k_f$ can support an inverse transfer and, at the same time, they can support a forward transfer at wavenumber $k \gg k_f$ for a range of values of the parameters (Alexakis & Biferale 2018). In generalised 2-D turbulence, the inverse transfer can be attributed to instabilities that couple the forced modes to large-scale 2-D modes, transferring energy to larger scales, which is typical for the $\alpha = 2$ model (Alexakis 2018). For $\alpha = 1$, the forward transfer can be attributed to the filament instabilities, which generate smaller scales (Held *et al.* 1995*b*; Scott & Dritschel 2014). A mechanism to inhibit the instability of a filament is the presence of a background strain due to a distant vortex. However, it has been found that the region of influence of the vortices decreases as we reduce α (see Iwayama & Watanabe 2010; Carton *et al.* 2016). This can explain why the forward flux of the generalised energy increases relative to the inverse flux as α decreases.

Figure 4 shows the generalised vorticity field for different values of α. For $\alpha = 2$, we get the array of vortices that are typically observed in 2-D Navier–Stokes, and are generated by the inverse cascade of energy. As α is reduced, we see that the vortices become diffused, with their sizes becoming larger. For $\alpha = 1$, Carton *et al.* (2016) found that the distance of vortex merging was generally smaller than for $\alpha = 2$. It was explained that for a point

https://doi.org/10.1017/jfm.2025.115 Published online by Cambridge University Press

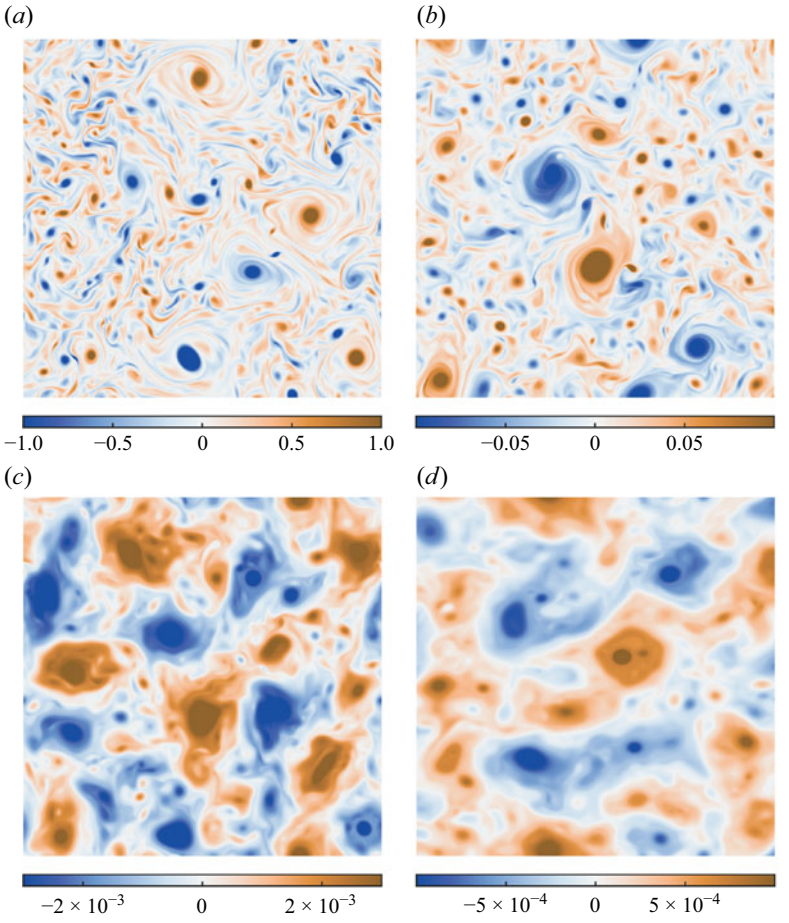


Figure 4. Generalised vorticity field for (*a*) $\alpha = 2.0$, (*b*) $\alpha = 1.0$, (*c*) $\alpha = -0.5$ and (*d*) $\alpha = -1.0$. For $\alpha = 2$, 1 and -0.5 the colourbar has been capped at 50 % of the maximum value and at 10 % for $\alpha = -1$ to emphasise the structures of the fields. The fields are obtained from DNS with $Re_+ = 1381$, $Re_- = 4 \times 10^7$ and $k_f = 16\sqrt{2}$.

vortex of the form $q(r) = \delta(r)$, where $\delta(r)$ is the Dirac delta function, the velocity field $\mathbf{u} \propto 1/r^2$ for the SQG model ($\alpha = 1$), while $\mathbf{u} \propto 1/r$ for the Navier–Stokes model ($\alpha = 2$) from the core of the vortex. Hence, the region of influence of the vortices decreases as we reduce α, which could explain the reduction in both vortex merging and inverse transfer of energy. To distinguish the behaviour of the generalised vorticity from the classical vorticity, we show in figure 5 the contour plots of the classical vorticity defined as $\omega = -\nabla^2\psi$ for all values of α. As seen from the plots, the classical vorticity goes to smaller length scales as α is reduced. For $\alpha < 0$, we observe a few vortices along with many filamentary structures, due to the forward cascade of generalised energy, that resemble the thin vortex filaments observed in 3-D Navier–Stokes turbulence (Ishihara *et al.* 2009).

3.2. *Near* $\alpha = 0$

Here we investigate the behaviour of the system close to $\alpha = 0$. At $\alpha = 0$, the nonlinearity vanishes and the flow becomes laminar. As one moves away from the threshold,

https://doi.org/10.1017/jfm.2025.115 Published online by Cambridge University Press

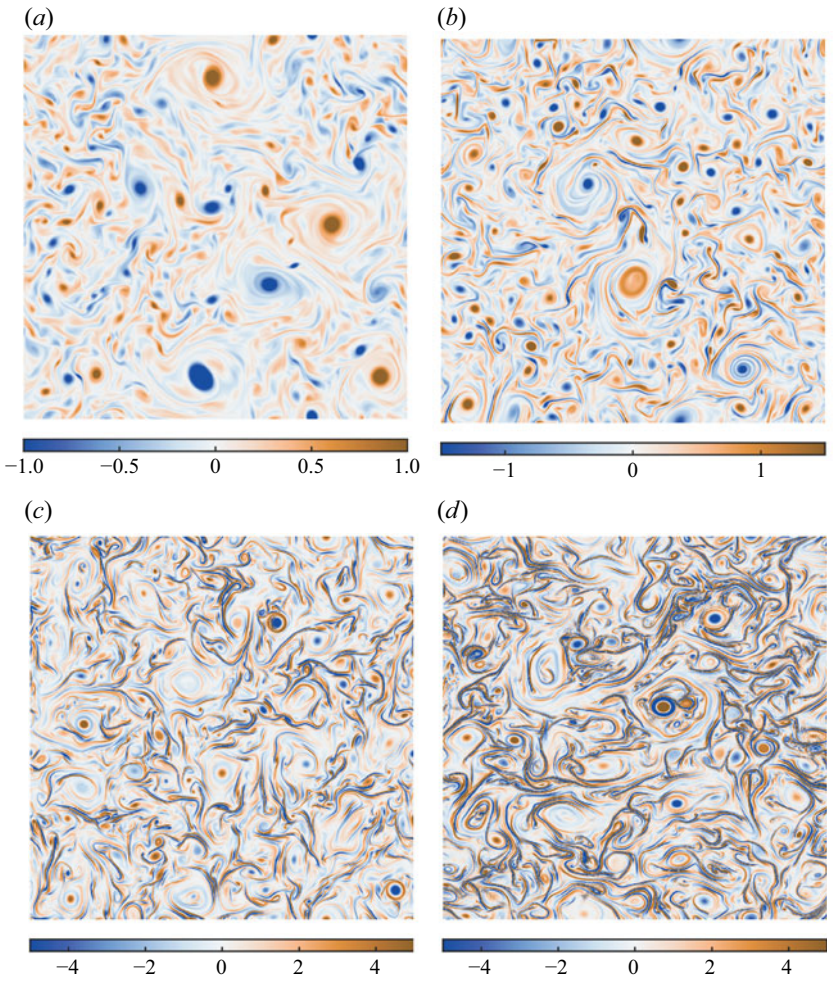


Figure 5. Classical vorticity field for (*a*) $\alpha = 2.0$, (*b*) $\alpha = 1.0$, (*c*) $\alpha = -0.5$ and (*d*) $\alpha = -1.0$. For $\alpha = 2$, 1 and -0.5 the colourbar has been capped at 50 % of the maximum value and at 10 % for $\alpha = -1$ to emphasise the structures of the fields. The fields are obtained from DNS with $Re_+ = 1381$, $Re_- = 4 \times 10^7$ and $k_f = 16\sqrt{2}$.

the flow remains laminar until it undergoes a linear instability. By numerically solving the eigenvalue problem of the linearised equations at small values of α, we find the primary instability to occur at length scales smaller than the laminar flow, unlike the negative viscosity instability that is observed in many 2-D flows (Sivashinsky & Yakhot 1985). This suggests that there is no inverse transfer of energy to scales larger than the forcing length scale for sufficiently small values of α. Inverse transfer of energy can be excited by secondary instabilities, as we move away from the primary instability threshold. The threshold of the primary instability is found to be the same for both positive and negative values of α. For convenience, we report on the critical point of the instability α_c as we increase α away from zero to positive values.

In figure 6, we show the critical point of the instability α_c as a function of Re_- and Re_+. For the parameters of $Re_+ = 1381$, $Re_- = 4 \times 10^7$ at $\alpha = 0$, the large-scale dissipation is negligible, and thus we find that the instability threshold α_c is almost independent of Re_- (see figure 6*a*). We also find that the threshold decreases like a power law as Re_+ increases

https://doi.org/10.1017/jfm.2025.115 Published online by Cambridge University Press

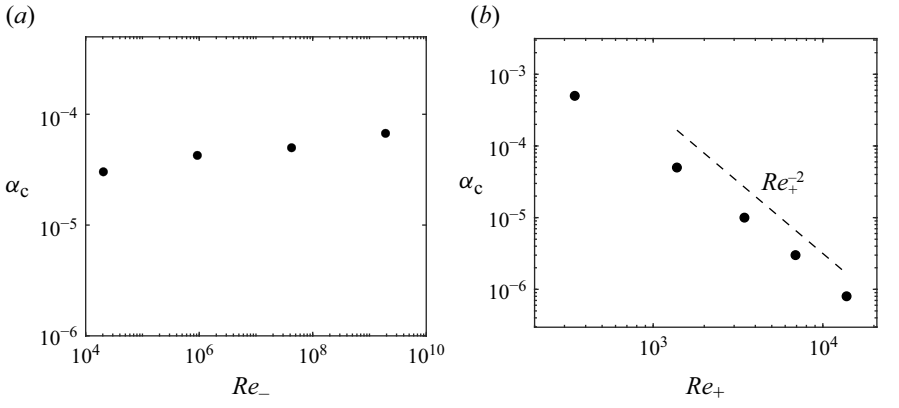


Figure 6. Variation of α_c as a function of (*a*) Re_- and (*b*) Re_+. The dashed line in panel (*b*) denotes the scaling $\alpha_c \propto Re_+^{-2}$.

(see figure 6*b*), and thus neglecting the effect of large-scale dissipation, we expect that $\alpha_c \to 0$ as $Re_+ \to \infty$. The dependence on Re_+ indicates that the behaviour very close to the critical point is sensitive to the hyper-viscous coefficient.

The scaling law of α_c with Re_+ we observe in figure 6 can be derived by doing a perturbation around $\alpha = 0$. Details of the perturbation analysis can be found in Appendix B. In essence, we perturb the laminar state and then we balance the nonlinear term with the small-scale dissipative term to obtain the following scaling law for the threshold of the instability

$$\alpha_c \propto Re_+^{-2}. \tag{3.1}$$

This scaling law is denoted by the dashed line in figure 6(*b*) and has a good agreement with the thresholds found numerically for different Re_+.

3.3. *Locality of cascades – α dependence*

Here we quantify the locality of the nonlinear triadic interactions by analysing the transfer rate of generalised energy transferred via the generalised vorticity advection term from one shell of wavenumbers $Q < k < Q + \Delta k$ to another shell of wavenumbers $K < k < K + \Delta k$. We define this shell-to-shell transfer function as

$$T_E(K, Q, t) = \langle \psi_K (\mathbf{u} \cdot \nabla q_Q) \rangle, \tag{3.2}$$

where ψ_K and q_Q are the streamfunction and generalised vorticity fields filtered such that only the wavenumbers at shell K and Q are kept, respectively. The transfer term $T_E(K, Q, t)$ conserves the generalised energy, i.e. it does not generate or destroy E_G, but it is responsible for the redistribution of the generalised energy across different scales. By construction, (3.2) transfers energy from ψ_K modes to q_Q modes and hence it is not anti-symmetric. This is also evident from the numerical results of figure 7(*a–d*). On the other hand, the shell-to-shell transfer of generalised enstrophy, from q_K modes to q_Q modes, is defined as

$$T_\Omega(K, Q, t) = \langle q_K (\mathbf{u} \cdot \nabla q_Q) \rangle. \tag{3.3}$$

Here, T_Ω is anti-symmetric under exchange of K and Q. This is also verified numerically (see figure 7*e–h*).

https://doi.org/10.1017/jfm.2025.115 Published online by Cambridge University Press

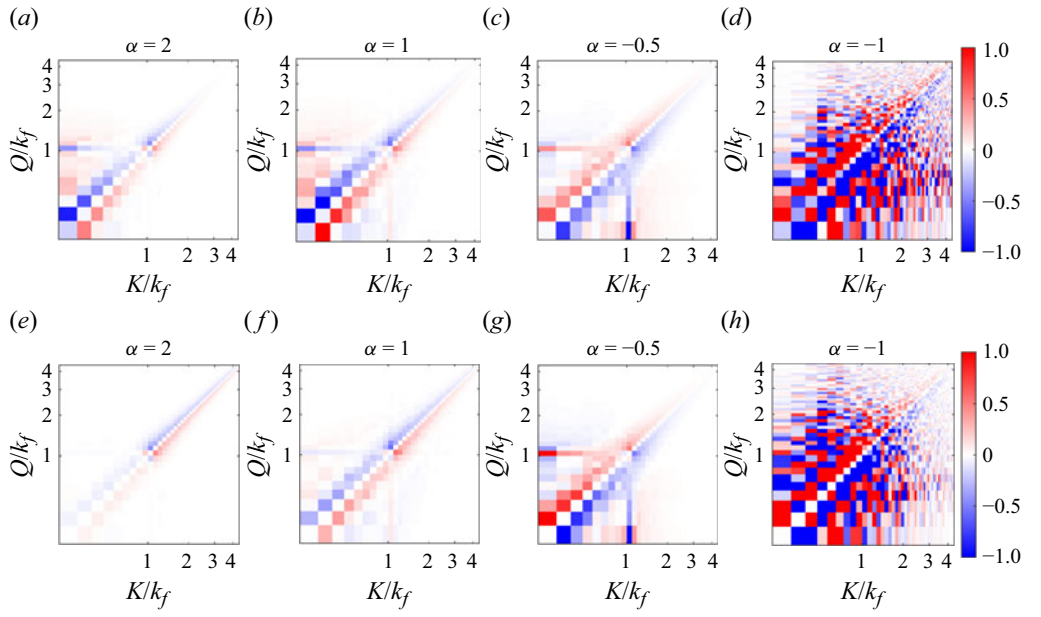


Figure 7. Shell-to-shell transfers of generalised energy as $T_E(K, Q)/\epsilon$ for (*a*) $\alpha = 2.0$, (*b*) $\alpha = 1.0$, (*c*) $\alpha = -0.5$ and (*d*) $\alpha = -1.0$. Shell-to-shell transfers of generalised enstrophy as $T_\Omega(K, Q)/\xi$ for (*e*) $\alpha = 2.0$, (*f*) $\alpha = 1.0$, (*g*) $\alpha = -0.5$ and (*h*) $\alpha = -1.0$. The colourbars are the same for all the plots and are shown only in plots (*d*) and (*h*) for clarity. The shell-to-shell transfers are obtained from DNS with $Re_+ = 1381$, $Re_- = 10^6$ and $k_f = 8\sqrt{2}$. The shell-to-shell transfers are averaged over at least 100 realisations after a stationary state is achieved for all values of α.

The contour plots in figures 7(*a*)–7(*d*) show the value of the time-averaged shell-to-shell transfer function $T_E(K, Q)$ normalised by the energy injection rate ϵ for $\alpha = 2.0$ in panel (*a*), $\alpha = 1.0$ in panel (*b*), $\alpha = -0.5$ in panel (*c*) and $\alpha = -1.0$ in panel (*d*). The K/k_f and Q/k_f axes are shown in logarithmic scale for better clarity of the range $K/k_f < 1$ and $Q/k_f < 1$. Local shell-to-shell transfers occur close to the diagonal $K = Q$, while non-local transfers occur away from the diagonal $K = Q$. For $\alpha = 2$, the shell-to-shell transfer $T_E(K, Q)/\epsilon$ is mostly concentrated at $K/k_f < 1$, $Q/k_f < 1$ and close to the diagonal $K = Q$, indicating that generalised energy cascades to large scales and mostly via local transfers. For values of $\alpha < 2$, we observe that the transfer becomes more significant at $K/k_f > 1$ and $Q/k_f > 1$, and this is because the cascade of E_G transitions gradually to small scales. Moreover, for $\alpha = 1$ and -0.5, the shell-to-shell transfer $T_E(K, Q)/\epsilon$ happens not only locally close to $K = Q$, but there are also two non-local branches, which become increasingly more significant as $\alpha \to -0.5$. These are the vertical branch, close to $K/k_f = 1$ along the wavenumbers $Q/k_f \lesssim 1$, and the horizontal branch, close to $Q/k_f = 1$ along the wavenumbers $K/k_f \lesssim 1$. At $\alpha = -1$, we find that $T_E(K, Q)/\epsilon$ is fully non-local spanning the whole range of wavenumbers.

In a similar fashion, the contour plots in figures 7(*e*)–7(*h*) show the time averaged shell-to-shell transfer function $T_\Omega(K, Q)$ normalised by the enstrophy injection rate ξ for $\alpha = 2.0$ in panel (*e*), $\alpha = 1.0$ in panel (*f*), $\alpha = -0.5$ in panel (*g*) and $\alpha = -1.0$ in panel (*h*),. For $\alpha = 2$, the shell-to-shell transfer $T_\Omega(K, Q)/\xi$ occurs predominantly at $K/k_f > 1$, $Q/k_f > 1$ and close to the diagonal $K = Q$, indicating that generalised enstrophy cascades to small scales through local interactions in wavenumber space. For values of $\alpha < 2$, we observe that $T_\Omega(K, Q)/\xi$ turns gradually to low wavenumbers, i.e. at $K/k_f < 1$ and $Q/k_f < 1$, and this happens since the cascade of Ω_G transitions to

https://doi.org/10.1017/jfm.2025.115 Published online by Cambridge University Press

large scales. In addition, for $\alpha = 1$ and -0.5, the shell-to-shell transfer happens via three branches. One local branch adjacent to $K = Q$ and two non-local branches, which become increasingly more significant as $\alpha \to -0.5$. Again these branches are the vertical and horizontal branches that have similar pattern to the non-local branches of $T_E(K, Q)/\epsilon$. Finally, at $\alpha = -1$, we also find that $T_\Omega(K, Q)/\xi$ is fully non-local spread across the wavenumbers.

The fact that the cascades of the generalised energy and enstrophy become gradually non-local as we go from positive to negative values of α is a notion clearly at variance with the typical locality assumption of the Kolmogorov phenomenology. This might be another reason why the energy spectra in figure 2 do not agree with the scaling predictions from (2.12) and (2.13).

4. Theoretical estimates

In this section, we discuss theoretical bounds on generalised energy and enstrophy dissipation rates, which we derive in Appendix C using exact mathematical inequalities. As we already described in § 3, the dissipation rates did not reach Reynolds-number-independent behaviour in our DNS, even at the highest Reynolds numbers examined (which required high spatial resolutions). Thus, we attempt to study the infinite Reynolds number behaviour of the dissipation rates theoretically, at the statistically stationary regime, using bounds. Moreover, we also consider the condensate regime, where reaching statistical stationarity is computationally very challenging, by ignoring the large-scale dissipation term.

Note that numerically, we used hyper- and hypo-viscous dissipation terms to reach high enough Reynolds numbers. Theoretically, though, we are not limited by computational power, and hence we derive the bounds using the standard dissipation terms. So, let us start with (2.1) and consider the small- and large-scale dissipation terms with $n = 1$ and $m = 0$, respectively, given by

$$\partial_t q + J(q, \psi) = \nu_+ \nabla^2 q - \nu_- q + f_q, \tag{4.1}$$

where f_q is a time-independent external forcing and broadband in the spectral domain. The above equation is studied in the domain $[0, 2\pi] \times [0, 2\pi]$ subject to periodic boundary conditions. The corresponding evolution equation for the streamfunction can be found using (2.2), i.e.

$$\partial_t \psi + J'(q, \psi) = \nu_+ \nabla^2 \psi - \nu_- \psi + f_\psi, \tag{4.2}$$

where $f_\psi = (-\nabla^2)^{-\alpha/2} f_q$ and $J'(q, \psi) = (-\nabla^2)^{-\alpha/2} J(q, \psi)$. We define the forcing wavenumber as $k_f = (\langle |\nabla^2 f_\psi|^2 \rangle / \langle |f_\psi|^2 \rangle)^{1/4}$, and the dimensionless measures of the generalised energy and enstrophy dissipation rates as

$$c_\epsilon = \frac{\epsilon_+}{U^3 k_f^{\alpha-1}}, \qquad c_\xi = \frac{\xi_+}{U^3 k_f^{2\alpha-1}}, \tag{4.3}$$

where $U = \langle |\mathbf{u}|^2 \rangle^{1/2} = \langle |\nabla \psi|^2 \rangle^{1/2}$ is the root-mean-square (r.m.s.) velocity and k_f is used for dimensional consistency. For the purposes of the analysis in Appendix C, it is more useful and convenient to define the Reynolds number based on the r.m.s. velocity instead of the forcing amplitude. This leads to the following definitions,

$$Re = \frac{U}{k_f \nu_+}, \qquad Rh = \frac{U k_f}{\nu_-}. \tag{4.4}$$

https://doi.org/10.1017/jfm.2025.115 Published online by Cambridge University Press

In what follows, we discuss the main results from the bounds. The technical details of the derivation are described in Appendix C. The $\alpha > 0$ and $\alpha < 0$ cases are discussed separately owing to the nature of the cascades, which is governed by the sign of α. Mathematically, the two cases arise because for $\alpha > 0$, generalised enstrophy is a higher order derivative quantity than generalised energy and *vice versa* for $\alpha < 0$. The idea for the bounds is that once the dissipative term with the highest order derivative is bounded, we then proceed to bound the other dissipative term (see Appendix C).

4.1. *Positive* α

Using the generalised enstrophy balance and assuming a statistically stationary state, we are able to bound the small-scale dissipation rate of generalised enstrophy (see Appendix C) as

$$\xi_+ \leqslant C_0 k_f^{2\alpha-1} U (C_1' U^2 + C_2' \nu_+ k_f U + C_3' \nu_- k_f^{-1} U), \tag{4.5}$$

where C_0, C_1', C_2', C_3' are constants that depend on the form of the forcing function and the domain geometry. The above equation in non-dimensional form can be written as

$$c_\xi \leqslant C_1 + C_2 Re^{-1} + C_3 Rh^{-1}, \tag{4.6}$$

where we have divided by $k_f^{2\alpha-1} U^3$, and used (4.3) and (4.4). So, as $Re \to \infty$ and $Rh \to \infty$, we find that for $0 < \alpha \leqslant 1$ and $\alpha = 2$, the generalised enstrophy dissipation rate c_ξ is bounded from above by a positive constant, which is independent of Re and Rh. This bound is an upper bound, which allows both for zero and finite c_ξ as a possible solution. So, (4.6) does not rule out a dissipation anomaly for the generalised enstrophy dissipation rate in the infinite Reynolds number limit.

Then, we proceed to bound the energy dissipation rate, where its dimensionless form is found to obey

$$c_\epsilon \leqslant Re^{-1/2} (C_5 + C_6 Re^{-1} + C_7 Rh^{-1})^{1/2}. \tag{4.7}$$

In this case, as $Re \to \infty$, we get $c_\epsilon \to 0$, since c_ϵ is positive definite, implying no forward cascade of generalised energy for $0 < \alpha \leqslant 1$ and $\alpha = 2$ in the infinite Reynolds number limit.

If we now consider no large-scale dissipation, a large-scale condensate is formed for $\alpha > 0$. In this case, considering $Rh \to \infty$ and $Re \to \infty$ in (4.7) and (4.6), we can claim that $c_\epsilon \to 0$ and the upper bound on c_ξ can allow for cascade solutions to exist.

4.2. *Negative* α

Using the generalised energy balance and assuming a statistically stationary state, we are able to bound the small-scale dissipation rate of generalised enstrophy (see Appendix C) as

$$\epsilon_+ \leqslant C k_f^{\alpha-1} U (\tilde{C}_1' U^2 + \tilde{C}_2' \nu_+ k_f U + \tilde{C}_3' \nu_- k_f^{-1} U), \tag{4.8}$$

where C, $\tilde{C}_1'$, $\tilde{C}_2'$, $\tilde{C}_3'$ are constants that depend on the forcing function and the domain parameters. Expressing the above equation in non-dimensional form gives

$$c_\epsilon \leqslant \tilde{C}_1 + \tilde{C}_2 Re^{-1} + \tilde{C}_3 Rh^{-1}, \tag{4.9}$$

where we have divided by $k_f^{\alpha-1} U^3$ and used (4.3) and (4.4). Thus, as $Re \to \infty$ and $Rh \to \infty$, we find that for $\alpha < 0$, the generalised energy dissipation rate c_ϵ is bounded from above by a constant independent of Re and Rh. Again, this expression is an upper

https://doi.org/10.1017/jfm.2025.115 Published online by Cambridge University Press

bound, which allows both for zero and finite c_ϵ as a possible solution. So, (4.9) does not rule out a dissipation anomaly for the generalised energy dissipation rate in the infinite Reynolds number limit.

Next, we find that the non-dimensional generalised enstrophy dissipation rate obeys

$$c_\xi \leqslant Re^{-1/2}\big(\tilde{C}_5 + \tilde{C}_6 Re^{-1} + \tilde{C}_7 Rh^{-1}\big)^{1/2}. \tag{4.10}$$

Thus, as $Re \to \infty$, we get $c_\xi \to 0$, since c_ξ is positive definite, implying no forward cascade of generalised enstrophy for $\alpha < 0$ in the infinite Reynolds number limit.

Again, if we now consider no large-scale dissipation, a large-scale condensate can be formed for $\alpha < 0$. Taking the limits $Rh \to \infty$ and $Re \to \infty$ in (4.9) and (4.10), we can claim that $c_\xi \to 0$ and the upper bound on c_ϵ can allow for cascade solutions to exist.

In summary, the bounds we derived for positive and negative α demonstrate that there is a transition of cascades between the generalised energy and enstrophy, if the upper bounds are taken to be exact. In other words, for $\alpha > 0$, the bounds suggest that in the infinite Reynolds number limit, $\epsilon_+ \to 0$ possibly due to the inverse cascade, and ξ_+ can remain finite due to the dissipation anomaly of the forward cascade, while the opposite is true for $\alpha < 0$.

5. Conclusion

In this paper, we focus on the numerical analysis of the cascades in generalised 2-D turbulence by systematically varying the parameter α of the model in the range $-1 \leqslant \alpha \leqslant 2$. The value and sign of α determines whether the cascade of a given quadratic invariant is inverse, forward or bidirectional. We find that there is a transition in the direction of the cascades as one varies the value of α. At the threshold $\alpha = 0$, the nonlinear term vanishes and the flow is laminar. We find that as we move away from $\alpha = 0$, the laminar flow undergoes a linear small wavelength instability at a critical value α_c, which is the same both for positive and negative α. We observe that $\alpha_c \approx$ const. as we increase Re_-; however, $\alpha_c \propto Re_+^{-2}$ as Re_+ increases. This scaling is also verified theoretically by doing a perturbation analysis.

Using mathematical inequalities for $0 < \alpha \leqslant 1$ and $\alpha = 2$, we are able to bound the dimensionless dissipation rates of generalised energy $c_\epsilon \equiv \epsilon/(U^3 k_f^{\alpha-1}) \leqslant Re^{-1/2}(C_5 + C_6 Re^{-1} + C_7 Rh^{-1})^{1/2}$ and enstrophy $c_\xi \equiv \xi/(U^3 k_f^{2\alpha-1}) \leqslant C_1 + C_2 Re^{-1} + C_3 Rh^{-1}$. In the limit of $Re \to \infty$, these bounds state that $c_\epsilon \to 0$, which can be related to the inverse cascade of E_G, while c_ξ can either become zero or finite due to the dissipation anomaly of the forward cascade of Ω_G. On the other hand, for $\alpha < 0$, we obtain the bounds $c_\epsilon \leqslant \tilde{C}_1 + \tilde{C}_2 Re^{-1} + \tilde{C}_3 Rh^{-1}$ and $c_\xi \leqslant Re^{-1/2}(\tilde{C}_5 + \tilde{C}_6 Re^{-1} + \tilde{C}_7 Rh^{-1})^{1/2}$. In this case, for $Re \to \infty$, the bounds give $c_\xi \to 0$, which can be related to the inverse cascade of Ω_G, while c_ϵ can either become zero or finite due to the dissipation anomaly of the forward cascade of E_G.

In numerical simulations, when $\alpha > 0$, the generalised energy E_G cascades inversely while generalised enstrophy Ω_G cascades forward, and the opposite happens when $\alpha < 0$ (see figure 1). Moreover, we find that the amount of dissipation rates of E_G and Ω_G depend on the system parameters Re_- and Re_+. This transition from positive to negative α is also clear from the spectral fluxes (see figure 3), which swap signs, indicating the transition of the cascades' direction. The energy spectra at large scales, i.e. at length scales larger than the forcing length scale, seem to agree with Kolmogorov type scalings of the generalised 2-D turbulence. However, this is not true for length scales smaller than the forcing length scale. A reason for this discrepancy might be that higher resolution computations are

https://doi.org/10.1017/jfm.2025.115 Published online by Cambridge University Press

required to shed light, or that the non-local transfers of generalised energy and enstrophy might be the cause of this disagreement. Finally, it is interesting to mention that due to the forward cascade of E_G for $\alpha < 0$, the classical vorticity field, which is dominated by vortex filaments, is reminiscent of the filaments observed in 3-D Navier–Stokes turbulence.

This study shows that the generalised model of 2-D turbulence is another convenient set-up to study the transition of turbulent cascades. However, this model is unique as it shows features that appear in 3-D turbulence, like the vortex filaments, emerging in two dimensions. So, further numerical studies at higher Reynolds numbers are required to deepen our understanding and relate the dynamics of the vortex filaments in two dimensions to the dissipation anomaly of generalised energy, if present, for negative values of α. Further mathematical analysis of this model dissipation anomaly for $\alpha < 0$ might provide new insights into the regularity of solutions of the 3-D Navier–Stokes equations. The study of locality of cascades using the shell-to-shell transfers from observational and experimental data of geophysical relevance would complement our findings, e.g. for the SQG model ($\alpha = 1$). Finally, the non-locality of cascades indicates that we should be thinking beyond the Kolmogorov type of arguments for these models.

Acknowledgment. We wish to thank Krishna Kumar for useful discussions and support. We also wish to thank the computing resources and support provided by PARAM Shakti supercomputing facility of IIT Kharagpur established under National Supercomputing Mission (NSM), Government of India and supported by Centre for Development of Advanced Computing (CDAC), Pune.

Funding. We acknowledge support from NSM Grant No. DST/NSM/R&D HPC Applications/2021/03.11, from the Institute Scheme from Innovative Research and Development (ISIRD), IIT Kharagpur, Grant No. IIT/SRIC/ISIRD/2021–2022/08 and the Start-up Research Grant No. SRG/2021/001229 from Science & Engineering Research Board (SERB), India.

Declaration of interests. The authors report no conflict of interest.

Appendix A. Numerical set-up

We perform DNS in a periodic square domain by numerically integrating the generalised vorticity equations (2.1) and (2.2) using the pseudospectral method (Gottlieb & Orszag 1977). We decompose the streamfunction $\psi(x, y, t)$ into basis functions of Fourier modes, *viz.*

$$\psi(\mathbf{x}, t) = \sum_{\mathbf{k}=-N/2}^{N/2} \widehat{\psi}_{\mathbf{k}}(t) e^{i\mathbf{k}\cdot\mathbf{x}}, \tag{A1}$$

where $\widehat{\psi}_{\mathbf{k}}$ is the amplitude of the $\mathbf{k} = (k_x, k_y)$ mode of ψ, and N denotes the number of aliased modes in the x and y directions. A third-order Runge–Kutta scheme is used for time advancement. The aliasing errors are removed with the 2/3 rule, which implies that the

	(*a*) $Re_+ = 1381$			(*b*) $Re_- = 4 \times 10^7$			
	$Re_-^{(1)} = 10^6$	$Re_-^{(2)} = 4 \times 10^7$	$Re_-^{(3)} = 2 \times 10^9$	$Re_+^{(1)} = 345$	$Re_+^{(2)} = 1381$	$Re_+^{(3)} = 3450$	$Re_+^{(4)} = 6900$
N	512^2	1024^2	2048^2	1024^2	1024^2	1024^2	1024^2
k_f	$8\sqrt{2}$	$16\sqrt{2}$	$32\sqrt{2}$	$16\sqrt{2}$	$16\sqrt{2}$	$16\sqrt{2}$	$16\sqrt{2}$

Table 1. Numerical parameters for the two set of runs corresponding to (*a*) fixed Re_+ with varying Re_- and (*b*) fixed Re_- with varying Re_+. N is the number of Fourier modes in our computations, Re_+ and Re_- are small- and large-scale Reynolds numbers, and k_f is the forcing wavenumber.

https://doi.org/10.1017/jfm.2025.115 Published online by Cambridge University Press

maximum wavenumber $k_{max} = N/3$. The numerical parameters we considered are listed in table 1. Time-averaged quantities are computed once the system has reached a statistically stationary regime. The computations were performed on graphics cards (GPUs), which provided three times speedup in contrast to computations on processors (CPUs).

Appendix B. Perturbation analysis

In this section, we look at the solutions from $\alpha = 0$ up to the critical point α_c. This region corresponds to the no-flux solution since the nonlinearity in the governing equation vanishes. As we go away from α_c, we can do a perturbation analysis knowing that the nonlinear terms are small compared with the linear dissipation terms, with α being the small parameter. For $|\alpha| \ll 1$, the solution is given by a laminar base flow ψ_b. This is the base flow around which the perturbation analysis will be carried out to find the α_c at which this solution loses stability. The laminar solution is obtained by balancing the hyper- and hypo-viscous terms with the forcing,

$$\psi_b = \frac{f_0}{\nu_+ k_f^4 + \nu_- k_f^{-4}} \sin(k_f x) \sin(k_f y), \tag{B1}$$

which is the solution for $|\alpha| < \alpha_c$.

As we cross the threshold α_c, we write the fields as a sum of the base flow and a perturbation, $q = q_b + \widetilde{q}$, $\psi = \psi_b + \widetilde{\psi}$, where the terms with the subscript $(\cdot)_b$ denote the base flow and the terms with $\widetilde{(.)}$ denote the perturbation fields. Substituting this decomposition into the nonlinear term of (2.1), we get

$$J(q, \psi) = J(q_b, \psi_b) + J(q_b, \widetilde{\psi}) + J\big(\widetilde{q}, \psi_b\big) + J\big(\widetilde{q}, \widetilde{\psi}, \big). \tag{B2}$$

The term $J(q_b, \psi_b)$ is zero for the laminar solution since q_b is linearly related to ψ_b and for the linear stability analysis, the term $J(\widetilde{q}, \widetilde{\psi})$ can be neglected as the term is second order in the amplitude of perturbations. Thus, by retaining only the linear terms in the perturbation fields, the nonlinear term in the governing equation (2.1) becomes

$$J(q, \psi) \approx J\big(q_b, \widetilde{\psi}\big) + J\big(\widetilde{q}, \psi_b\big). \tag{B3}$$

We first express the generalised vorticities q_b and $\widetilde{q}$ in terms of their respective streamfunctions ψ_b and $\widetilde{\psi}$. The forcing is at a single wavenumber, and thus based on (2.2), we can write

$$\widehat{q_b}(\mathbf{k}, t) = k_f^\alpha \widehat{\psi_b}(\mathbf{k}, t), \tag{B4}$$

where the $\widehat{(\cdot)}$ denotes Fourier coefficients. Similarly, the perturbation field $\widetilde{q}$ can be written as

$$\begin{aligned}
\widehat{\widetilde{q}}(\mathbf{k}, t) &= k^\alpha \widehat{\widetilde{\psi}}(\mathbf{k}, t) \\
&= k_f^\alpha \Big(1 + \alpha \log\Big(\frac{k}{k_f}\Big) + \mathcal{O}\big(\alpha^2\big)\Big) \widehat{\widetilde{\psi}}(\mathbf{k}, t) \\
&= k_f^\alpha \widehat{\widetilde{\psi}}(\mathbf{k}, t) + \alpha \widehat{\widetilde{Q}}(\,\mathbf{k}, t) + \mathcal{O}\big(\alpha^2\big)
\end{aligned} \tag{B5}$$

with $k^\alpha = k_f^\alpha (1 + \alpha \log(k/k_f) + O(\alpha^2))$ expanded in the limit of $\alpha \to 0$ and

$$\widehat{\widetilde{Q}}(\mathbf{k}, t) = k_f^\alpha \log\Big(\frac{k}{k_f}\Big) \widehat{\widetilde{\psi}}(\mathbf{k}, t). \tag{B6}$$

https://doi.org/10.1017/jfm.2025.115 Published online by Cambridge University Press

Using (B4) and (B6) in real space and substituting them into (B3), we get

$$J(q,\psi) \approx k_f^{\alpha} J\left(\psi_b, \widetilde{\psi}\right) + k_f^{\alpha} J\left(\widetilde{\psi}, \psi_b\right) + \alpha J\left(\widetilde{Q}, \psi_b\right). \tag{B7}$$

The first two terms cancel out each other with only the third term remaining which is proportional to α.

Now we can derive a scaling for α_c with Re_+ from the balance between the nonlinear term $\alpha J(\widetilde{Q}, \psi_b)$ and the hyper-viscous dissipation term $-\nu_+(-\nabla^2)^n\widetilde{\psi}$ with $n=2$. At the threshold α_c of the linear instability, we use (B1) and (B6) to find the following leading order scaling:

$$J(q,\psi) \propto \alpha_c \frac{f_0}{\nu_+ k_f^2}\, g_1\left(\frac{k_i}{k_f}\right)\widetilde{\psi}, \tag{B8}$$

$$\nu_+\nabla^4\widetilde{\psi} \propto \nu_+ k_f^4\, g_2\left(\frac{k_i}{k_f}\right)\widetilde{\psi}, \tag{B9}$$

where k_i denotes the typical wavenumber of the unstable mode $\widetilde{\psi}$ and g_1, g_2 are two functions of k_i/k_f. Equating (B8) with (B9), we get

$$\alpha_c \frac{f_0}{\nu_+ k_f^2} \propto \nu_+ k_f^4\, g_3\left(\frac{k_i}{k_f}\right), \tag{B10}$$

where g_3 is a function of k_i/k_f. We find that the ratio k_i/k_f remains almost constant as we vary Re_+ over a few decades, which leads to the following scaling law for the threshold of the instability:

$$\alpha_c \propto Re_+^{-2}. \tag{B11}$$

Appendix C. Bounds

Here, we derive the upper bounds for the non-dimensionalised dissipation rates defined in (4.3). We start by reproducing the definitions from § 4, with the (4.1) reproduced below,

$$\partial_t q + J(q,\psi) = \nu_+\nabla^2 q - \nu_- q + f_q, \tag{C1}$$

where f_q is the external forcing function which is taken to be a general smooth function that is time independent. The corresponding evolution equation for the streamfunction using (2.2) is also reproduced below, i.e.

$$\partial_t \psi + J'(q,\psi) = \nu_+\nabla^2\psi - \nu_-\psi + f_\psi, \tag{C2}$$

where $f_\psi = (-\nabla^2)^{-\alpha/2} f_q$ and the forcing wavenumber is defined as $k_f = (\langle|\nabla^2 f_\psi|^2\rangle/\langle|f_\psi|^2\rangle)^{1/4}$. We recall that

$$J'(q,\psi) = \left(-\nabla^2\right)^{-\alpha/2} J(q,\psi). \tag{C3}$$

The dimensionless measures of the generalised energy and enstrophy dissipation rates are given by $c_\epsilon = \epsilon_+/(U^3 k_f^{\alpha-1})$, $c_\xi = \xi_+/(U^3 k_f^{2\alpha-1})$, taken from (4.3). Here, $U = \langle|\mathbf{u}|^2\rangle^{1/2} = \langle|\nabla\psi|^2\rangle^{1/2}$ is the r.m.s. velocity and k_f is used for dimensional consistency. The Reynolds number based on the r.m.s. velocity defined in (4.4) are given by $Re = (U/k_f\nu_+)$, $Rh = (Uk_f/\nu_-)$. Note that the Reynolds number defined here is based on the r.m.s. velocity. To obtain the upper bound estimates, we start with bounding the dissipative term with

https://doi.org/10.1017/jfm.2025.115 Published online by Cambridge University Press

the highest order derivative. From this estimate, we then bound the other dissipative term. Since the nature of the cascades is governed by the sign of α, we consider the two cases separately.

C.1 *Positive* α

In the statistically stationary state, we have the generalised enstrophy balance, $\xi_+ + \xi_- = \xi$, discussed in (2.7), which can be similarly derived from (C1), where $\xi_+ = \nu_+\langle|\nabla q|^2\rangle$, $\xi_- = \nu_-\langle q^2\rangle$ and $\xi = \langle q f_q\rangle$. From the enstrophy balance and (2.8), we can write

$$\xi_+ = \langle q f_q\rangle - \nu_-\langle q^2\rangle \leqslant C' k_f^{2\alpha}\langle|\psi|^2\rangle^{1/2}\langle|f_\psi|^2\rangle^{1/2} - \nu_-\langle q^2\rangle, \tag{C4}$$

$$\leqslant C' k_f^{2\alpha}\langle|\psi|^2\rangle^{1/2} F_\psi, \tag{C5}$$

where $F_\psi = \langle|f_\psi|^2\rangle^{1/2}$ is the forcing amplitude and C' is a constant. Here, we have applied the Cauchy–Schwarz inequality to the first term, $k_f^{2\alpha}\langle\psi f_\psi\rangle$, and $\nu_-\langle q^2\rangle$ is a positive definite quantity, and hence it can be neglected from the upper bound estimate. Since ψ is a lower derivative than the velocity field $\mathbf{u}$, we can use the Poincaré inequality (Doering & Gibbon 1995) to write

$$\begin{aligned}\langle|\psi|^2\rangle^{1/2} &\leqslant C k_f^{-1}\langle|\mathbf{u}|^2\rangle^{1/2}\\ &\leqslant C k_f^{-1} U,\end{aligned} \tag{C6}$$

where C is a constant that depends on the domain geometry. Combining (C5) with (C6) yields a bound on the small-scale dissipation rate of generalised enstrophy in terms of the forcing amplitude, i.e.

$$\xi_+ \leqslant C_0 k_f^{2\alpha-1} U F_\psi. \tag{C7}$$

where C_0 is a constant. Now, we would like to replace F_ψ in terms of the r.m.s. velocity, which will help us obtain the bound in terms of the dimensionless dissipation rate c_ξ, as it is defined based on the r.m.s. velocity. For this, we follow Alexakis & Doering (2006) and multiply (C2) by a smoothly varying, time independent function ϕ, giving

$$\phi\partial_t\psi + \phi J'(q,\psi) = \nu_+\phi\nabla^2\psi - \nu_-\phi\psi + \phi f_\psi. \tag{C8}$$

Performing spatiotemporal averaging and changing the order of differentiation using integration by parts, we get

$$\langle\phi J'(q,\psi)\rangle - \nu_+\langle\psi\nabla^2\phi\rangle + \nu_-\langle\phi\psi\rangle = \langle\phi f_\psi\rangle, \tag{C9}$$

since $\langle\phi\partial_t\psi\rangle = 0$ due to statistical stationarity. Let us derive estimates for each term separately. For the second and third terms on the left-hand side of (C9), we can use the Cauchy–Schwarz inequality and (C6) to write

$$\begin{aligned}-\nu_+\langle\psi\nabla^2\phi\rangle &\leqslant \nu_+\langle|\psi|^2\rangle^{1/2}\langle|\nabla^2\phi|^2\rangle^{1/2}\\ &\leqslant \nu_+ C k_f^{-1} U\langle|\nabla^2\phi|^2\rangle^{1/2},\end{aligned} \tag{C10}$$

and

$$\begin{aligned}\nu_-\langle\phi\psi\rangle &\leqslant \nu_-\langle|\phi|^2\rangle^{1/2}\langle|\psi|^2\rangle^{1/2}\\ &\leqslant \nu_-\langle|\phi|^2\rangle^{1/2} C k_f^{-1} U.\end{aligned} \tag{C11}$$

https://doi.org/10.1017/jfm.2025.115 Published online by Cambridge University Press

For the first term of (C9), using (C3), we can write

$$\begin{aligned}\langle \phi J'(q,\psi)\rangle &= \langle \phi(-\nabla^2)^{-\frac{\alpha}{2}} J(q,\psi)\rangle \\ &= \langle \phi(-\nabla^2)^{-\frac{\alpha}{2}}(\mathbf{u}\cdot\nabla)q\rangle. \end{aligned} \tag{C12}$$

We proceed to simplify this expression by using the incompressibility condition of the velocity field and the periodicity of the domain. After some simplifications, we get

$$\begin{aligned}\langle \phi J'(q,\psi)\rangle &= \left\langle \phi\nabla\cdot\left((-\nabla^2)^{-\frac{\alpha}{2}}(\mathbf{u}q)\right)\right\rangle \\ &= -\langle[(-\nabla^2)^{\frac{-\alpha}{2}}(\nabla\phi)].(\mathbf{u}q)\rangle. \end{aligned} \tag{C13}$$

Now, we apply Hölder's inequality to get

$$\begin{aligned}\langle \phi J'(q,\psi)\rangle &\leqslant ||\left(-\nabla^2\right)^{-\alpha/2}\nabla\phi||_\infty ||\mathbf{u}||_2||q||_2 \\ &\leqslant ||\left(-\nabla^2\right)^{-\alpha/2}\nabla\phi||_\infty C U^2 k_f^{-1+\alpha}, \end{aligned} \tag{C14}$$

where the $||.||_2$ term denotes the L_2 norm and C is a constant that depends on the form of the forcing function and domain geometry. In the last step, we have used the relation $||q||_2 \leqslant CUk_f^{-1+\alpha}$ for $0\leqslant\alpha\leqslant 1$. For $\alpha=2$, we obtain a similar bound as in Alexakis & Doering (2006). The infinity norm is defined as $||\theta||_\infty = \max|\theta(x,y)|$, which gives the maximum absolute value of a function θ over the domain.

Putting (C14), (C10) and (C11) in (C9), we get

$$\langle \phi f_\psi\rangle \leqslant ||\left(-\nabla^2\right)^{-\frac{\alpha}{2}}\nabla\phi||_\infty C k_f^{-1+\alpha}U^2 + C\nu_+\left\langle|\nabla^2\phi|^2\right\rangle^{1/2}k_f^{-1}U + C\nu_-\left\langle|\phi|^2\right\rangle^{1/2}k_f^{-1}U. \tag{C15}$$

By letting $\phi = f_\psi/F_\psi$ and using the definition $k_f^2 = \langle|\nabla^2 f_\psi|^2\rangle^{1/2}/\langle|f_\psi|^2\rangle^{1/2}$, we can simplify (C15) and obtain a bound relating the forcing amplitude F_ψ and the r.m.s. velocity. In the first term on the right-hand side, the infinity norm simplifies to $k_f^{1-\alpha}$ times a constant which depends on the shape of the forcing function, the second term on the right-hand side becomes $C\nu_+k_f^2k_f^{-1}U$ and the last term becomes $C\nu_-k_f^{-1}U$, where the constants depend on the form of forcing function and geometry. Eventually, (C15) turns into the following expression:

$$F_\psi \leqslant C_1'U^2 + C_2'\nu_+k_fU + C_3'\nu_-k_f^{-1}U, \tag{C16}$$

where C_1', C_2', C_3' are constants that depend on the form of the forcing function and the domain geometry. Substituting (C16) in the expression for the generalised enstrophy dissipation rate (C7), we obtain the following bound:

$$\xi_+ \leqslant C_0k_f^{2\alpha-1}U\left(C_1'U^2 + C_2'\nu_+k_fU + C_3'\nu_-k_f^{-1}U\right), \tag{C17}$$

which in non-dimensional form can be written as

$$c_\xi \leqslant C_1 + C_2Re^{-1} + C_3Rh^{-1}, \tag{C18}$$

where we have divided by $k_f^{2\alpha-1}U^3$ and used (4.3) and (4.4).

Now we have obtained a bound on the generalised enstrophy dissipation rate, we then look to bound the generalised energy dissipation rate given by $\epsilon_+ = -\nu_+\langle\psi\nabla^2q\rangle$. Using the Cauchy–Schwarz inequality, we get

https://doi.org/10.1017/jfm.2025.115 Published online by Cambridge University Press

$$\epsilon_+ \leqslant \nu_+ \langle |\nabla\psi|^2 \rangle^{1/2} \langle |\nabla q|^2 \rangle^{1/2}$$
$$\leqslant C_4 \nu_+^{1/2} U \xi_+^{1/2}, \tag{C19}$$

since $U = \langle |\mathbf{u}|^2 \rangle^{1/2} = \langle |\nabla\psi|^2 \rangle^{1/2}$ and $\xi_+ = \nu_+ \langle |\nabla q|^2 \rangle$. Using the bound for ξ_+ from (C17) and dividing by $U^3 k_f^{\alpha-1}$, this inequality simplifies to

$$c_\epsilon \leqslant Re^{-1/2} \left(C_5 + C_6 Re^{-1} + C_7 Rh^{-1} \right)^{1/2}. \tag{C20}$$

C.2 *Negative* α

We follow a similar approach for negative α. In the statistically stationary state, we have the generalised energy balance, $\epsilon_+ + \epsilon_- = \epsilon$ discussed in (2.6), which can be similarly derived from (C1), where $\epsilon_+ = -\nu_+ \langle \psi \nabla^2 q \rangle$, $\epsilon_- = \nu_- \langle \psi q \rangle$ and $\epsilon = \langle \psi f_q \rangle$. Using the generalised energy balance, we can write

$$\epsilon_+ = \langle \psi f_q \rangle - \nu_- \langle \psi q \rangle. \tag{C21}$$

Using the Cauchy–Schwarz inequality to the first term, we get

$$\epsilon_+ \leqslant \langle |\psi|^2 \rangle^{1/2} \langle |f_q|^2 \rangle^{1/2} - \nu_- \langle \psi q \rangle$$
$$\leqslant \langle |\psi|^2 \rangle^{1/2} \langle |f_q|^2 \rangle^{1/2}, \tag{C22}$$

where $F_q = \langle |f_q|^2 \rangle^{1/2}$ is another measure of the forcing amplitude related to F_ψ and the large-scale dissipative term $\nu_- \langle \psi q \rangle$ is positive definite, so it can be removed from the upper bound estimate in (C22). We can then apply Poincaré inequality to the first term as ψ is a lower derivative than $\mathbf{u}$ and write

$$\langle |\psi|^2 \rangle^{1/2} \leqslant C k_f^{-1} \langle |\mathbf{u}|^2 \rangle^{1/2}$$
$$\leqslant C k_f^{-1} U, \tag{C23}$$

where C is a constant which depends on the domain geometry and the forcing function. Combining (C22) and (C23), we can write

$$\epsilon_+ \leqslant C k_f^{-1} U F_q. \tag{C24}$$

Now, we multiply (C1) by a smoothly varying, time independent function ϕ, to give

$$\phi \partial_t q + \phi J(q, \psi) = \nu_+ \phi \nabla^2 q - \nu_- \phi q + \phi f_q. \tag{C25}$$

By performing spatiotemporal averaging and changing the order of differentiation using integration by parts, we get

$$\langle \phi J(q, \psi) \rangle - \nu_+ \langle q \nabla^2 \phi \rangle + \nu_- \langle \phi q \rangle = \langle \phi f_q \rangle \tag{C26}$$

as $\langle \phi \partial_t q \rangle = 0$ due to statistical stationarity. We can use the Fourier space relation (2.8) between q and ψ along with (C6) to write

$$\langle |q|^2 \rangle^{1/2} \leqslant \tilde{C} k_f^{\alpha} \langle |\psi|^2 \rangle^{1/2}$$
$$\leqslant \tilde{C} k_f^{\alpha-1} U, \tag{C27}$$

where $\tilde{C}$ is another constant that depends on the domain geometry and the forcing function. We now look to bound each term on the left-hand side of (C26) separately. For the second

https://doi.org/10.1017/jfm.2025.115 Published online by Cambridge University Press

and third terms, we can use Cauchy–Schwarz inequality and (C27) to get

$$-\nu_+\langle q\nabla^2\phi\rangle \leqslant \nu_+\langle|q|^2\rangle^{1/2}\langle|\nabla^2\phi|^2\rangle^{1/2} \leqslant \nu_+\tilde{C}k_f^{\alpha-1}U\langle|\nabla^2\phi|^2\rangle^{1/2} \tag{C28}$$

and

$$\nu_-\langle\phi q\rangle \leqslant \nu_-\langle|\phi|^2\rangle^{1/2}\langle|q|^2\rangle^{1/2} \leqslant \nu_-\langle|\phi|^2\rangle^{1/2}\tilde{C}k_f^{\alpha-1}U. \tag{C29}$$

For the first term on the left-hand side of (C26), we use the Hölder and Cauchy–Schwarz inequalities along with (C27) to get

$$\langle\phi J(q,\psi)\rangle = -\langle(\mathbf{u}\cdot\nabla\phi)q\rangle \leqslant ||\nabla\phi||_\infty\langle|q|^2\rangle^{1/2}\langle|\mathbf{u}|^2\rangle^{1/2} \leqslant ||\nabla\phi||_\infty\tilde{C}k_f^{\alpha-1}U^2. \tag{C30}$$

Putting (C28), (C29) and (C30) back in (C26), we get

$$\langle\phi f_q\rangle \leqslant \tilde{C}||\nabla\phi||_\infty k_f^{\alpha-1}U^2 + \tilde{C}\nu_+k_f^{\alpha-1}U\langle|\nabla^2\phi|^2\rangle^{1/2} + \tilde{C}\nu_-\langle|\phi|^2\rangle^{1/2}k_f^{\alpha-1}U. \tag{C31}$$

Now, by letting $\phi = f_q/F_q$, we can simplify the expression in a similar manner to positive α and obtain a bound relating the forcing amplitude F_q with the r.m.s. velocity, *viz.*

$$F_q \leqslant k_f^\alpha\big(\tilde{C}_1'U^2 + \tilde{C}_2'\nu_+k_fU + \tilde{C}_3'\nu_-k_f^{-1}U\big), \tag{C32}$$

where $\tilde{C_1}'$, $\tilde{C_2}'$ and $\tilde{C_3}'$ are constants that depend on the form of the forcing function and the domain geometry. Substituting (C32) in the expression for the generalised energy dissipation rate (C24), we obtain the following bound:

$$\epsilon_+ \leqslant Ck_f^{\alpha-1}U\big(\tilde{C}_1'U^2 + \tilde{C}_2'\nu_+k_fU + \tilde{C}_3'\nu_-k_f^{-1}U\big), \tag{C33}$$

which, in non-dimensional form, can be written as

$$c_\epsilon \leqslant \tilde{C}_1 + \tilde{C}_2Re^{-1} + \tilde{C}_3Rh^{-1}, \tag{C34}$$

obtained after dividing by $k_f^{\alpha-1}U^3$ and using (4.3) and (4.4).

We then look to bound the generalised enstrophy dissipation rate $\xi_+ = \nu_+\langle|\nabla q|^2\rangle$, which can be written in the spectral space as

$$\xi_+ = \nu_+\sum_{\mathbf{k}} k^{1+\frac{\alpha}{2}}k^{1-\frac{\alpha}{2}}|\widehat{q}(\mathbf{k},t)|^2. \tag{C35}$$

Using the Cauchy–Schwarz inequality, we get the expression

$$\xi_+ \leqslant \nu_+\left(\sum_{\mathbf{k}} k^{2+\alpha}|\widehat{q}(\mathbf{k},t)|^2\right)^{\frac{1}{2}}\left(\sum_{\mathbf{k}} k^{2-\alpha}|\widehat{q}(\mathbf{k},t)|^2\right)^{\frac{1}{2}}. \tag{C36}$$

For the first term in the brackets, we can use (2.8) along with the inequality $k^\alpha \leqslant C'k_f^\alpha$, valid for negative values of α, to get

$$\left(\sum_{\mathbf{k}} k^{2+\alpha}|\widehat{q}(\mathbf{k},t)|^2\right)^{\frac{1}{2}} = \left(\sum_{\mathbf{k}} k^{2+3\alpha}|\widehat{\psi}(\mathbf{k},t)|^2\right)^{\frac{1}{2}} \leqslant \tilde{C}_4k_f^{3\alpha/2}U, \tag{C37}$$

https://doi.org/10.1017/jfm.2025.115 Published online by Cambridge University Press

where $\tilde{C}_4$ is a constant that depends on the form of the forcing function and the domain geometry. Now, the second term in the brackets of (C36) can be written as

$$\Big(\sum_{\mathbf{k}} k^{2-\alpha}|\widehat{q}(\mathbf{k},t)|^2\Big)^{\frac{1}{2}} = \big\langle q\nabla^2\psi\big\rangle^{1/2} = (\epsilon_+/\nu_+)^{1/2}, \tag{C38}$$

using again (2.8). Putting (C37) and (C38) back in (C36), we get

$$\xi_+ \leqslant \tilde{C}_4 \nu_+^{1/2} k_f^{3\alpha/2} U \epsilon_+^{1/2}. \tag{C39}$$

Using the bound for ϵ_+ from (C33), this inequality simplifies to

$$c_\xi \leqslant Re^{-1/2}\big(\tilde{C}_5 + \tilde{C}_6 Re^{-1} + \tilde{C}_7 Rh^{-1}\big)^{1/2} \tag{C40}$$

in non-dimensional form.

References

Alexakis, A. 2011 Two-dimensional behavior of three-dimensional magnetohydrodynamic flow with a strong guiding field. *Phys. Rev.* E **84** (5), 056330.

Alexakis, A. 2018 Three-dimensional instabilities and negative eddy viscosity in thin-layer flows. *Phys. Rev. Fluids* **3** (11), 114601.

Alexakis, A. 2023 Quasi-two-dimensional turbulence. *Rev. Mod. Plasma Phys.* **7** (1), 31.

Alexakis, A. & Biferale, L. 2018 Cascades and transitions in turbulent flows. *Phys. Rep.* **767–769**, 1–101.

Alexakis, A. & Biferale, L. 2022 λ-Navier–Stokes turbulence. *Phil. Trans. R. Soc. Lond. A: Math. Phys. Engng Sci.* **380**, 20210243.

Alexakis, A. & Doering, C.R. 2006 Energy and enstrophy dissipation in steady state 2d turbulence. *Phys. Lett. A* **359** (6), 652–657.

Arbic, B.K., Polzin, K.L., Scott, R.B., Richman, J.G. & Shriver, J.F. 2013 On eddy viscosity, energy cascades, and the horizontal resolution of gridded satellite altimeter products. *J. Phys. Oceanogr.* **43** (2), 283–300.

Balwada, D., LaCasce, J.H. & Speer, K.G. 2016 Scale-dependent distribution of kinetic energy from surface drifters in the Gulf of Mexico. *Geophys. Res. Lett.* **43** (20), 10–856.

Balwada, D., Xie, J.-H., Marino, R. & Feraco, F. 2022 Direct observational evidence of an oceanic dual kinetic energy cascade and its seasonality. *Sci. Adv.* **8** (41), eabq2566.

Benavides, S.J. & Alexakis, A. 2017 Critical transitions in thin layer turbulence. *J. Fluid Mech.* **822**, 364–385.

Boffetta, G. & Ecke, R.E. 2012 Two-dimensional turbulence. *Annu. Rev. Fluid Mech.* **44** (1), 427–451.

Boffetta, G. & Musacchio, S. 2010 Evidence for the double cascade scenario in two-dimensional turbulence. *Phys. Rev.* E **82** (1), 016307.

Byrne, D. & Zhang, J.A. 2013 Height-dependent transition from 3-D to 2-D turbulence in the hurricane boundary layer. *Geophys. Res. Lett.* **40** (7), 1439–1442.

Campagne, A., Gallet, B., Moisy, F. & Cortet, P.-P. 2014 Direct and inverse energy cascades in a forced rotating turbulence experiment. *Phys. Fluids* **26** (12), 125112.

Carton, X., Ciani, D., Verron, J., Reinaud, J. & Sokolovskiy, M. 2016 Vortex merger in surface quasi-geostrophy. *Geophys. Astrophys. Fluid Dyn.* **110** (1), 1–22.

Celani, A., Musacchio, S. & Vincenzi, D. 2010 Turbulence in more than two and less than three dimensions. *Phys. Rev. Lett.* **104** (18), 184506.

Chan, C.-k., Mitra, D. & Brandenburg, A. 2012 Dynamics of saturated energy condensation in two-dimensional turbulence. *Phys. Rev.* E **85** (3), 036315.

Deusebio, E., Boffetta, G., Lindborg, E. & Musacchio, S. 2014 Dimensional transition in rotating turbulence. *Phys. Rev.* E **90** (2), 023005.

Doering, C.R. & Gibbon, J.D. 1995 *Applied Analysis of the Navier–Stokes Equations*. Cambridge University Press.

Ecke, R.E. 2017 From 2D to 3D in fluid turbulence: unexpected critical transitions. *J. Fluid Mech.* **828**, 1–4.

Fjørtoft, R. 1953 On the changes in the spectral distribution of kinetic energy for twodimensional, nondivergent flow. *Tellus* A: *Dyn. Meteorol. Oceanogr.* **5** (3), 225–230.

Foussard, A., Berti, S., Perrot, X. & Lapeyre, G. 2017 Relative dispersion in generalized two-dimensional turbulence. *J. Fluid Mech.* **821**, 358–383.

https://doi.org/10.1017/jfm.2025.115 Published online by Cambridge University Press

FRISCH, U., LESIEUR, M. & SULEM, P.L. 1976 Crossover dimensions for fully developed turbulence. *Phys. Rev. Lett.* **37** (14), 895–897.
GOTTLIEB, D. & ORSZAG, S.A. 1977 *Numerical Analysis of Spectral Methods: Theory and Applications*. SIAM. Society for Industrial and Applied Mathematics Philadelphia.
HELD, I.M., PIERREHUMBERT, R.T., GARNER, S.T. & SWANSON, K.L. 1995*a* Surface quasi-geostrophic dynamics. *J. Fluid Mech.* **282**, 1–20.
HELD, I.M., PIERREHUMBERT, R.T., GARNER, S.T. & SWANSON, K.L. 1995*b* Surface quasi-geostrophic dynamics. *J. Fluid Mech.* **282**, 1–20.
ISHIHARA, T., GOTOH, T. & KANEDA, Y. 2009 Study of high–reynolds number isotropic turbulence by direct numerical simulation. *Annu. Rev. Fluid Mech.* **41** (1), 165–180.
IWAYAMA, T., MURAKAMI, S. & WATANABE, T. 2015 Anomalous eddy viscosity for two-dimensional turbulence. *Phys. Fluids*. **27** (4), 045104.
IWAYAMA, T. & WATANABE, T. 2010 Green's function for a generalized two-dimensional fluid. *Phys. Rev.* E **82** (3), 036307.
VAN KAN, A. 2024 Phase transitions in anisotropic turbulence. *Chaos* **34** (12), 122103.
VAN KAN, A. & ALEXAKIS, A. 2020 Critical transition in fast-rotating turbulence within highly elongated domains. *J. Fluid Mech.* **899**, A33.
KHATRI, H., SUKHATME, J., KUMAR, A. & VERMA, M.K. 2018 Surface ocean enstrophy, kinetic energy fluxes, and spectra from satellite altimetry. *J. Geophys. Res.: Oceans* **123** (5), 3875–3892.
KING, G.P., VOGELZANG, J. & STOFFELEN, A. 2015 Upscale and downscale energy transfer over the tropical Pacific revealed by scatterometer winds. *J. Geophys. Res.: Oceans* **120** (1), 346–361.
KOLMOGOROV, A.N. 1941 The local structure of turbulence in incompressible viscous fluid for very large Reynolds number. *Dokl. Akad. Nauk SSSR* **30**, 301.
KRAICHNAN, R.H. 1971 Inertial-range transfer in two-and three-dimensional turbulence. *J. Fluid Mech.* **47** (3), 525–535.
KRAICHNAN, R.H. 1976 Eddy viscosity in two and three dimensions. *J. Atmos. Sci.* **33** (8), 1521–1536.
LAPEYRE, G. 2017 Surface quasi-geostrophy. *Fluids* **2** (1), 7.
LARICHEV, V.D. & MCWILLIAMS, J.C. 1991 Weakly decaying turbulence in an equivalent-barotropic fluid. *Phys. Fluids* A **3** (5), 938–950.
LESUR, G. & LONGARETTI, P.-Y. 2011 Non-linear energy transfers in accretion discs MRI turbulence. *Astron. Astrophys.* **528**, A17.
LILLY, D.K. 1969 Numerical simulation of two-dimensional turbulence. *Phys. Fluids* **12** (12), II–240.
MARINO, R., MININNI, P.D., ROSENBERG, D. & POUQUET, A. 2013 Inverse cascades in rotating stratified turbulence: fast growth of large scales. *Europhys. Lett.* **102** (4), 44006.
NASTROM, G., GAGE, K. & JASPERSON, W. 1984 Kinetic energy spectrum of large-and mesoscale atmospheric processes. *Nature* **310** (5972), 36–38.
PIERREHUMBERT, R.T., HELD, I.M. & SWANSON, K.L. 1994*a* Spectra of local and nonlocal two-dimensional turbulence. *Chaos, Solitons Fractals* **4** (6), 1111–1116.
PIERREHUMBERT, R.T., HELD, I.M. & SWANSON, K.L. 1994*b* Spectra of local and nonlocal two-dimensional turbulence. *Chaos, Solitons Fractals* **4** (6), 1111–1116.
READ, P.L. 2001 Transition to geostrophic turbulence in the laboratory, and as a paradigm in atmospheres and oceans. *Surv. Geophys.* **22** (3), 265–317.
RHINES, P.B. 1979 Geostrophic turbulence. *Annu. Rev. Fluid Mech.* **11** (1), 401–441.
SCOTT, R.B. & WANG, F. 2005 Direct evidence of an oceanic inverse kinetic energy cascade from satellite altimetry. *J. Phys. Oceanogr.* **35** (9), 1650–1666.
SCOTT, R. K. & DRITSCHEL, D. 2014 Numerical simulation of a self-similar cascade of filament instabilities in the surface quasigeostrophic system. *Phys. Rev. Lett.* **112** (14), 144505.
SEN, A., MININNI, P.D., ROSENBERG, D. & POUQUET, A. 2012 Anisotropy and nonuniversality in scaling laws of the large-scale energy spectrum in rotating turbulence. *Phys. Rev.* E **86** (3), 036319.
SESHASAYANAN, K., BENAVIDES, S.J. & ALEXAKIS, A. 2014*a* On the edge of an inverse cascade. *Phys. Rev.* E **90** (5), 051003.
SESHASAYANAN, K., BENAVIDES, S.J. & ALEXAKIS, A. 2014*b* On the edge of an inverse cascade. *Phys. Rev.* E **90** (5), 051003.
SHAO, X., ZHANG, N. & TANG, J. 2023 A physical model for the observed inverse energy cascade in typhoon boundary layers. *Geophys. Res. Lett.* **50** (18), 264501.
SHATS, M., BYRNE, D. & XIA, H. 2010 Turbulence decay rate as a measure of flow dimensionality. *Phys. Rev. Lett.* **105** (26), 264501.
SIEGELMAN, L., *et al.* 2022 Moist convection drives an upscale energy transfer at Jovian high latitudes. *Nat. Phys.* **18** (3), 357–361.

https://doi.org/10.1017/jfm.2025.115 Published online by Cambridge University Press

SIVASHINSKY, G. & YAKHOT, V. 1985 Negative viscosity effect in large-scale flows. *Phys. Fluids* **28** (4), 1040–1042.

SMITH, K., BOCCALETTI, G., HENNING, C., MARINOV, I., TAM, C., HELD, I. & VALLIS, G. 2002 Turbulent diffusion in the geostrophic inverse cascade. *J. Fluid Mech.* **469**, 13–48.

SMITH, L.M., CHASNOV, J.R. & WALEFFE, F. 1996 Crossover from two-to three-dimensional turbulence. *Phys. Rev. Lett.* **77** (12), 2467–2470.

SOZZA, A., BOFFETTA, G., MURATORE-GINANNESCHI, P. & MUSACCHIO, S. 2015 Dimensional transition of energy cascades in stably stratified forced thin fluid layers. *Phys. Fluids* **27** (3), 035112.

TABELING, P. 2002 Two-dimensional turbulence: a physicist approach. *Phys. Rep.* **362** (1), 1–62.

TEITELBAUM, T. & MININNI, P.D. 2012 Thermalization and free decay in surface quasigeostrophic flows. *Phys. Rev.* E **86** (1), 016323.

TRAN, C.V. 2004 Nonlinear transfer and spectral distribution of energy in α turbulence. *Phys.* D: *Nonlinear Phenom.* **191** (1-2), 137–155.

VERMA, M.K. 2024 Critical dimension for hydrodynamic turbulence. *Phys. Rev.* E **110** (3), 035102.

WATANABE, T. & IWAYAMA, T. 2004 Unified scaling theory for local and non-local transfers in generalized two-dimensional turbulence. *J. Phys. Soc. Japan* **73** (12), 3319–3330.

WATANABE, T. & IWAYAMA, T. 2007 Interacting scales and triad enstrophy transfers in generalized two-dimensional turbulence. *Phys. Rev.* E **76** (4), 046303.

XIA, H., BYRNE, D., FALKOVICH, G. & SHATS, M. 2011 Upscale energy transfer in thick turbulent fluid layers. *Nat. Phys.* **7** (4), 321–324.

YOUNG, R.M. & READ, P.L. 2017 Forward and inverse kinetic energy cascades in Jupiter's turbulent weather layer. *Nat. Phys.* **13** (11), 1135–1140.

https://doi.org/10.1017/jfm.2025.115 Published online by Cambridge University Press